J. Fluid Mech. (2021), *vol*. 913, A11, doi:10.1017/jfm.2020.1171

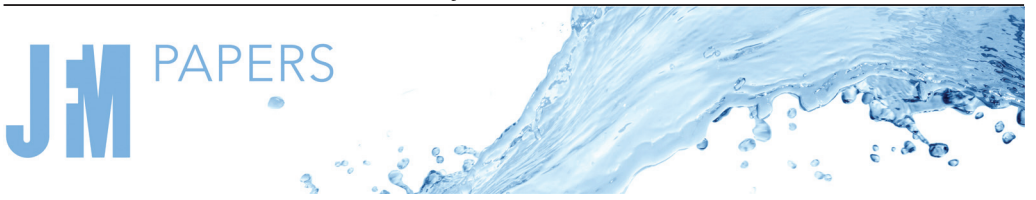

2-D and 3-D measurements of flame stretch and turbulence–flame interactions in turbulent premixed flames using DNS

Haiou Wang[1],†, Evatt R. Hawkes[2,3], Jiahao Ren[1], Guo Chen[1], Kun Luo[1] and Jianren Fan[1]

[1]State Key Laboratory of Clean Energy Utilization, Zhejiang University, Hangzhou 310027, PR China

[2]School of Mechanical and Manufacturing Engineering, The University of New South Wales, NSW 2052, Australia

[3]School of Photovoltaic and Renewable Energy Engineering, The University of New South Wales, NSW 2052, Australia

(Received 21 June 2020; revised 27 October 2020; accepted 21 December 2020)

Three-dimensional (3-D) measurements of flame stretch are experimentally challenging. In this paper, two-dimensional (2-D) and 3-D measurements of flame stretch and turbulence–flame interactions were examined using direct numerical simulation (DNS) data of turbulent premixed flames, and models to estimate 3-D statistics of flame stretch-related quantities by correcting 2-D measurements were developed. A variety of DNS cases were simulated, including three freely propagating planar flames without a mean shear and a slot-jet flame with a mean shear. The main findings are summarized as follows. First, the mean shear mainly influences the flame orientations. However, it does not change the flame stretch and turbulence–flame interactions qualitatively. The distributions of out-of-plane angle of all cases are nearly isotropic. Second, models were proposed to approximate the 3-D statistics of flame stretch-related quantities using 2-D measurements, the performance of which was verified by comparing modelled and actual 3-D surface averages and probability density functions of tangential strain rate, curvature and displacement velocity. Third, 2-D measurements of flame stretch capture properly the trends of the 3-D results, with flame surface area being produced in low curvature regions and destroyed in highly curved regions. However, the magnitude of flame stretch was under-estimated in 2-D measurements. Finally, 2-D and 3-D turbulence–flame interactions were examined. The flame normal vector is aligned with the most compressive strain rate in both 2-D and 3-D measurements. Meanwhile, the flame normal vector is misaligned

† Email address for correspondence: wanghaiou@zju.edu.cn

(weakly aligned) with the most extensive strain rate in 3-D (2-D) measurements, highlighting the difference in 2-D and 3-D results of turbulence–flame interactions.

Key words: combustion, flames, turbulent reacting flows

1. Introduction

Flame stretch is a topic that has received considerable interest in the premixed combustion community (Pope 1988; Candel & Poinsot 1990; Cant, Pope & Bray 1990; Trouve & Poinsot 1994; Vervisch *et al.* 1995; Kollmann & Chen 1998; Wang *et al.* 2017*b*; Luca *et al.* 2019). The flame stretch is defined as the rate of change of flame surface area and can be written as (Candel & Poinsot 1990; Cant *et al.* 1990; Wang *et al.* 2017*b*)

$$\frac{\delta \dot{A}}{\delta A} = (\delta_{ij} - n_i n_j)\frac{\partial \dot{X}_i}{\partial x_j}, \tag{1.1}$$

where δA is an infinitesimal element of the flame surface area, n_i is the ith component of the flame normal vector, $\dot{X}_i$ is the ith component of the velocity of a point $\boldsymbol{X}$ on the surface in an isosurface following reference frame and is given by $\dot{X}_i = u_i + S_d n_i$, where u_i is the ith component of the flow velocity and S_d is the displacement velocity. In the flamelet regime, the flame surface density approach has been proposed for combustion modelling (Candel & Poinsot 1990; Cant *et al.* 1990; Trouve & Poinsot 1994). The transport equation of the flame surface density Σ is

$$\frac{\partial \Sigma}{\partial t} + \nabla \cdot (\langle \dot{X} \rangle_s \Sigma) = \left\langle (\delta_{ij} - n_i n_j)\frac{\partial \dot{X}_i}{\partial x_j} \right\rangle_s \Sigma, \tag{1.2}$$

where $\langle \cdot \rangle_s$ denotes surface averaging, as will be further explained in § 3. It is obvious that flame stretch is connected closely with the flame surface density. The closure of models for the flame surface density equation was investigated in the context of large-eddy simulation (known as LES) by Hawkes & Cant (2000, 2001). Although the equation above was originally developed with the intention of applications in the flamelet regime, it is exact and does not require a flamelet assumption. Thus, it is still applicable to describe the evolution of a flame that is not thin. Recently, Wang *et al.* (2017*b*) examined flame stretch in a laboratory premixed flame in the broken reaction zones regime, and insights into flame stretch of highly turbulent flames were revealed. Luca *et al.* (2019) conducted DNS of four slot-jet flames in the thin reaction zones regime at increasing Reynolds number, and found that the contributions of different components of flame stretch are largely independent of the Reynolds number when scaled by the Kolmogorov time scale. There has been an increasing interest in combustion modes such as lean premixed combustion (Dunn-Rankin 2007), where relatively weak flames interact with intense turbulence, so that these flames are located in the thin or broken reaction zones regime. The review of Driscoll *et al.* (2020) and a number of direct numerical simulation (DNS) studies (Lapointe & Blanquart 2017; Wang *et al.* 2017*c*, 2018; Nilsson *et al.* 2019) showed that flamelet models could also be valid in a wider range of conditions than previously believed. However, some recent experimental studies have shown limitations of the flamelet assumption for highly turbulent premixed flames (Mohammadnejad *et al.* 2019, 2020). Therefore, improved understanding of fundamental aspects of flame stretch is critical to develop advanced combustion models for highly turbulent flames.

Flame stretch-related quantities, such as tangential strain rate (Donbar, Driscoll & Carter 2001; Steinberg & Driscoll 2009; Zhang *et al.* 2011; Steinberg, Driscoll & Swaminathan 2012; Sponfeldner *et al.* 2015; Steinberg, Coriton & Frank 2015), curvature (Lee, North & Santavicca 1992; Anselmo-Filho *et al.* 2009; Steinberg & Driscoll 2009; Wang *et al.* 2013) and displacement velocity (Hartung *et al.* 2009; Trunk *et al.* 2013), have been measured extensively using experiments. In these studies, the flame location and structure is typically determined by planar laser-induced florescence (PLIF) (Lee *et al.* 1992; Donbar *et al.* 2001; Anselmo-Filho *et al.* 2009; Hartung *et al.* 2009; Steinberg & Driscoll 2009; Zhang *et al.* 2011; Steinberg *et al.* 2012; Trunk *et al.* 2013; Wang *et al.* 2013; Sponfeldner *et al.* 2015; Steinberg *et al.* 2015), while velocities are typically determined by particle-image velocimetry (PIV) (Donbar *et al.* 2001; Zhang *et al.* 2011) or stereoscopic PIV (Hartung *et al.* 2009; Steinberg & Driscoll 2009; Steinberg *et al.* 2012; Trunk *et al.* 2013; Sponfeldner *et al.* 2015; Steinberg *et al.* 2015). Measuring three-component quantities in two-dimensional (2-D) planes has been attempted. For example, (Trunk *et al.* 2013) used dual-plane OH PLIF and stereoscopic PIV to compute the local displacement velocity of freely propagating premixed flames. Particularly, the flame was identified in each pair of PLIF images. The fitted flame surface between the PLIF images was used to determine the three components of flame orientation, which then was used to evaluate the displacement velocity in a measuring plane. Sponfeldner *et al.* (2015) used crossed-plane OH-PLIF to measure the three components of the flame normal vector. Due to the difficulty of three-dimensional (3-D) measurements, most of these experiments were performed in two spatial dimensions, where the gradient of flow velocities and scalars in the third direction is not accessible. The 3-D measuring of flame stretch-related quantities using experiments is, therefore, very challenging. Alternatively, the 3-D statistics of flame stretch-related quantities could be obtained by correcting 2-D measurements, which motivates the present work.

There have been few DNS studies in the literature exploring the relationship between 2-D and 3-D statistics of turbulent flames. Hawkes *et al.* (2009) developed models for 3-D scalar dissipation probability density function (PDF) to be reconstructed from lower-dimensional approximations. Veynante *et al.* (2010*a*) proposed and evaluated several models to obtain 3-D averages of flame surface density from 2-D measurements, with excellent agreement being achieved by comparing with DNS data where 3-D quantities are known. Later, models were proposed to approximate 3-D averages using 2-D measurements of quantities related to transport equations of flame surface density by Hawkes, Sankaran & Chen (2011) and scalar dissipation rate by Chakraborty *et al.* (2013). Chakraborty *et al.* (2011) demonstrated the strengths and limitations of the predictive capabilities of the planar imaging techniques in the measurement of displacement velocity. Despite the above-mentioned works, to the best of our knowledge, there has been no systematic study of the relationship between 2-D and 3-D statistics of flame stretch and its related quantities.

The orientation of flame normal vector to principal strain rates of the flow affects the tangential strain rate, a component of flame stretch. Previous studies of turbulence–flame interactions exploited the alignment characteristics between the flame normal vector and principal strain rates using DNS (Swaminathan & Grout 2006; Chakraborty & Swaminathan 2007; Kim & Pitsch 2007; Cifuentes *et al.* 2014; Wang, Hawkes & Chen 2016). In general, the flame normal vector aligns with the most extensive (compressive) strain rate in weakly (highly) turbulent flames. The alignments of flame normal vector and principal strain rates have also been studied experimentally (Hartung *et al.* 2008; Steinberg *et al.* 2012; Sponfeldner *et al.* 2015), where the trends are consistent with those in the DNS.

However, it is unclear to what extent the 2-D measurements agree with the actual 3-D results, which are not accessible from experimental measurements. This paper is going to explore the relationship between 2-D and 3-D turbulence–flame interactions and quantify their difference using DNS.

In this context, the objective of the present study is, therefore, to explore the 2-D and 3-D measurements of flame stretch and turbulence–flame interactions using DNS of turbulent premixed flames characterized by different levels of turbulence. Two DNS configurations are employed, including freely propagating planar flames without a mean shear and slot-jet flames with a mean shear. The present paper is organized as follows. Section 2 describes the DNS configuration and numerical methods employed in the present study. Section 3 introduces the mathematical background of this work. The results are presented and discussed in § 4. Finally, conclusions are made in § 5.

2. Simulation details

In this section, the numerical details of the two configurations are first given, respectively, followed by a brief description of the solver.

2.1. *Freely propagating planar premixed flames*

For the freely propagating planar flames (figure 1*a*), inflow and outflow boundary conditions are used in the streamwise direction x, and periodic boundary conditions are used in the lateral directions y and z. The reactants consist of lean CH_4/air mixture with a temperature of 300 K and an equivalence ratio of 0.7 (Wang *et al.* 2016; Wang, Hawkes & Chen 2017*a*; Wang *et al.* 2017*b*). Under these conditions, the laminar flame velocity S_L is 0.19 m s^{-1}, the laminar flame thermal thickness δ_L is 0.66 mm and the laminar flame time τ_L is 3.47 ms. The inflow velocity is constant and its value approaches the turbulent flame velocity, so that the flame position remains stationary in the computational domain.

The simulations were initialized with a corresponding laminar premixed flame solution and a homogeneous isotropic turbulence field based on a prescribed Passot–Pouquet energy spectrum (Passot & Pouquet 1987). Three cases, i.e. case L, case M and case H, with different turbulent intensities were considered, where 'L', 'M' and 'H' refer to the level of turbulence (low, medium and high). The simulation parameters are listed in table 1, where l_t is the turbulence integral length scale, u' is the turbulent velocity and τ_e is the eddy turn-over time. The ratio of the turbulence integral length scale to flame thickness, l_t/δ_L, is 1.0, which is of similar order as that found in a slot burner flame (Sankaran *et al.* 2007) and in a recent highly turbulent jet flame (Wang *et al.* 2017*b*). The turbulent Reynolds number is defined as $Re = u' l_t/\nu$, where ν is the viscosity. The Karlovitz number is defined as $Ka = \tau_L/\tau_\eta$, where $\tau_\eta = (\nu l_t/u'^3)^{1/2}$ is the Kolmogorov time scale. In the Peters regime diagram (Peters 2000), case L is located in the thin reaction zones regime, while case M and case H are in the broken reaction zones regime. A linear forcing method was employed (Carroll & Blanquart 2016) to maintain a statistically stationary turbulent flame. The turbulent forcing was applied everywhere except for the boundaries in the streamwise direction to prevent the interaction of forcing with the inflow/outflow physical boundaries. Note that both of the forcing and flames were initialized at the beginning of the DNS. The flames reach a statistically steady state after the initial period, and statistical results presented in the paper are collected when the flames are statistically steady. It is found that turbulence parameters such as turbulent kinetic energy do not vary much in the vicinity of the flames compared with those in the upstream of the flames. Therefore, the interactions

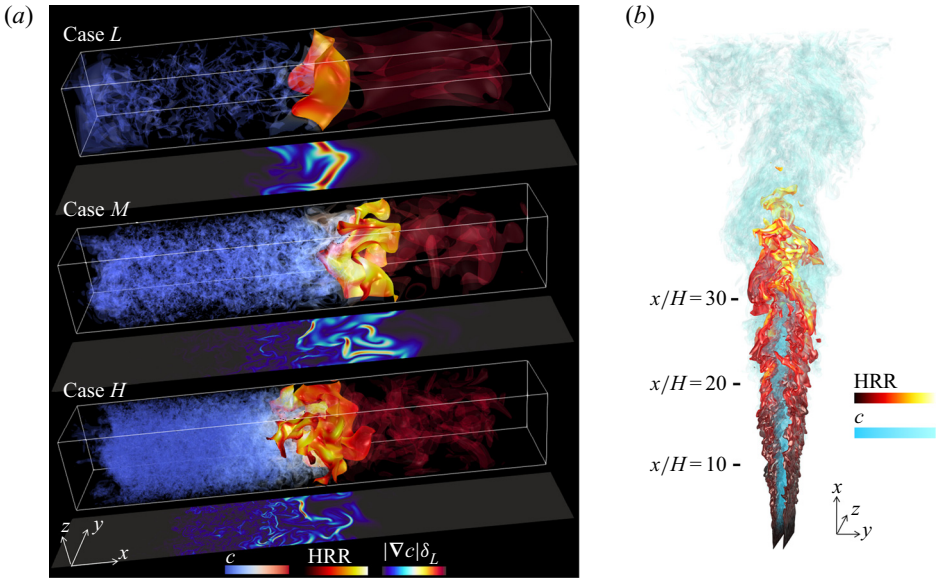

Figure 1. (*a*) Isosurface of vorticity magnitude ($\omega = \omega_{max}/30$) coloured by the progress variable c and isosurface of $c = 0.8$ coloured by heat release rate (HRR) for freely propagating planar flames, where ω_{max} is the maximum value of the vorticity magnitude in the domain. The range of c is from 0 to 1 and the range of HRR is from 0.4×10^9 to 2.0×10^9 J m^{-3} s^{-1} for all three cases. The slices show 2-D distributions of the surface density function $|\nabla c|$. The range of $|\nabla c|\delta_L$ is from 0 to 0.4 for case L, to 0.9 for case M and to 1.7 for case H. (*b*) Three-dimensional rendering of the progress variable c and the isosurface of $c = 0.8$ coloured by HRR for the slot-jet flame. The range of c is from 0 to 1 and the range of HRR is from 0 to 1.9×10^9 J m^{-3} s^{-1}.

Case	u' (m s^{-1})	l_t (mm)	τ_e (ms)	Re	Ka
L	0.78	0.66	0.85	33	38
M	3.88	0.66	0.17	163	390
H	9.70	0.66	0.07	408	1710

Table 1. Simulation parameters of the planar flames.

of turbulence and the flames could be characterized using the turbulence parameters in the reactants.

The computational domain is $L_x \times L_y \times L_z = 6L \times L \times L$ in the streamwise direction x and lateral directions y and z, respectively, where L is 3.14 mm. The grid resolution is chosen to properly resolve all the flame and turbulence scales. Uniform grids were used in all directions and the number of grids is $N_x \times N_y \times N_z = 768 \times 128 \times 128$ for case L and case M with a grid size of 24.5 μm. In order to resolve the small-scale turbulence structures of case H, the grid number is increased to $N_x \times N_y \times N_z = 1344 \times 224 \times 224$ with a grid size of 14.0 μm. There is more than 0.5 grid for all cases to resolve the smallest turbulence scale, i.e. the Kolmogorov scale η. Note that the laminar flame thickness is 0.66 mm, so that the DNS grids are sufficient for the flames.

A reduced chemical mechanism for premixed CH_4/air flames with NO was employed (Lu & Law 2008). The reduced mechanism, based on GRI-Mech3.0, contains 268 elementary reactions and 44 species, of which 28 species were transported on the

Case	s_L (m s^{-1})	δ_L (mm)	Re ($u'l_t/s_L\delta_L$)	Da ($s_L l_t/u'\delta_L$)
J	1.7	0.374	38	0.42

Table 2. Simulation parameters of the slot-jet flame.

DNS grid. The mechanism has been used and validated in previous DNS studies (Wang *et al.* 2017*b*). Constant species Lewis numbers (Le), determined from a fit to mixture-averaged transport properties in a premixed flame, were employed for transport properties (Wang *et al.* 2017*b*).

2.2. *Slot-jet premixed flames*

The configuration of the slot-jet flame consists of a coflow and a central jet (figure 1*b*). The coflow of the DNS is generated from lean C_3H_8/air combustion with an equivalence ratio of 0.87, and the coflow temperature is 1500 K. The thermochemical conditions of the central jet are determined by adiabatically mixing the coflow and a cold jet (C_2H_4/air mixture with a temperature of 300 K and an equivalence ratio of 1.2). The resultant equivalence ratio of the central jet, ϕ_j, is 1.07. The temperature of the central jet, T_j, is 823 K. This DNS case is denoted as 'case J'.

The jet velocity U_j is 163 m s^{-1} and the coflow velocity U_c is 7.6 m s^{-1}. The mean velocity profile at the inlet is given as

$$U = U_j + \frac{U_c - U_j}{2}\left[1 + \tanh\left(\frac{y - H/2}{\delta}\right)\tanh\left(\frac{y + H/2}{\delta}\right)\right], \tag{2.1}$$

where the jet width H is 1.5 mm, and the shear layer thickness δ is specified as $0.1H$. The jet Reynolds number based on U_j and H is $Re_j = 2880$. The profile of a scalar ψ (temperature or species mass fractions) at the inlet is similar to that in Wang *et al.* (2017*b*) with a smooth transition between the jet and the coflow. A turbulence field is obtained by generating an auxiliary homogeneous isotropic turbulence. The turbulent velocity u' is 10 % of U_j for both cases and the integral length scale l_t is the same as H, i.e. 1.5 mm. The isotropic turbulence field is then filtered outside of the jet and added to the mean inlet velocity using Taylor's hypothesis. The other simulation parameters are listed in table 2.

The computational domain is $L_x \times L_y \times L_z = 60H \times 40H \times 10H$ in the streamwise x, traverse y and spanwise z directions, respectively. The grid spacing is chosen to resolve the flame and turbulence structures. Particularly, a uniform grid with $\Delta x = 50$ μm and $\Delta z = 37.5$ μm is used in the streamwise and spanwise directions, respectively. A stretched grid is used in the y direction with $\Delta y = 37.5$ μm in the region between $y/H = -5$ and 5, and gradually stretched outside of this region. There is at least 0.5 grid point across the Kolmogorov scale, η, throughout the computational domain, satisfying the criterion for resolving turbulence scales. The resultant number of grids is $N_x \times N_y \times N_z = 1800 \times 800 \times 400$. The boundary conditions are periodic in the spanwise direction and non-reflecting in other directions.

A reduced mechanism for C_2H_4 combustion including 206 elementary reactions and 32 species was used (Luo *et al.* 2012). This mechanism has been validated for various problems including autoignition and premixed flame propagation. The simulations were advanced for $3\tau_j$ after reaching a statistically steady state, where τ_j is the flow-through time estimated as $\tau_j = L_x/U_j$.

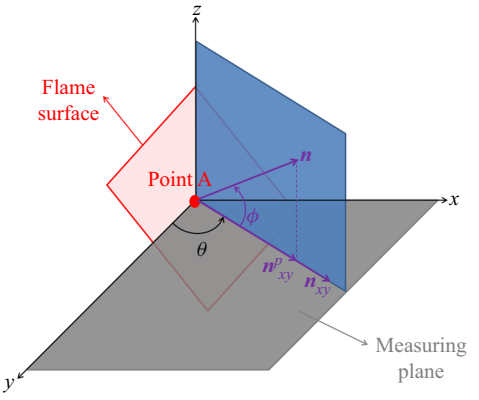

Figure 2. Schematic of the coordinate system.

2.3. *DNS solver*

In all simulations, the DNS code S3D (Chen *et al.* 2009) was employed to solve the compressible transport equations for continuity, momentum, species mass fractions and total energy. The code uses a fourth-order Runge–Kutta method for time integration and a skew-symmetric, eighth-order explicit finite difference spatial scheme (Kennedy & Carpenter 1994; Kennedy, Carpenter & Lewis 2000). A tenth-order filter was applied every 10 time steps to damp high-wavenumber oscillations. Improved Navier–Stokes characteristic boundary conditions (known as NSCBC) were used to prescribe the inflow and outflow boundary conditions (Yoo & Im 2007).

3. Mathematical background

3.1. *The coordinate system*

We consider a flame element in a coordinate system described in figure 2. The flame normal vector is denoted as $\boldsymbol{n}$, which is calculated as

$$\boldsymbol{n} = -\nabla c/|\nabla c|, \tag{3.1}$$

where c is the progress variable based on mass fractions of O_2 for freely propagating planar flames and H_2O for the slot-jet flame. The value of c increases monotonically from zero in the reactants to unity in the products. Sensitivity analyses of the results based on different definitions of the progress variable were carried out by Wang *et al.* (2017*a*) for understanding high *Ka* flame structures and by Lipatnikov *et al.* (2020) for flamelet modelling of turbulent premixed flames with various *Ka*. In general, the selection of species for calculating the progress variable does not have significant impact on the trends of the results reported in these studies, though quantitative difference was observed. In the present work, we focus on the statistics of various quantities related to flame stretch and turbulence–flame interactions, with the results being little affected by this selection.

By definition, the flame normal vector points towards the reactants. In a 3-D coordinate system, the flame normal vector could be rewritten as $\boldsymbol{n} = \boldsymbol{n}(n_x, n_y, n_z)$, where n_x, n_y and n_z are components of the flame normal vector. In 2-D analysis, the x–y plane is taken as the measuring plane unless otherwise specified, where velocities and scalars such as progress variable and species mass fractions can be accessed in the plane. No information in the z direction is used. Note that the mean direction of flame propagation aligns with x for

freely propagating planar flames, while it mostly aligns with y for the slot-jet flame, so the x–y plane captures properly the mean behaviour of the flames. The projection of the flame normal vector in the measuring plane is $\boldsymbol{n}_{xy}^{p}$ with $\boldsymbol{n}_{xy}^{p} = \boldsymbol{n}_{xy}^{p}(n_x, n_y)$ which is unknown from planar measurement, and the unit vector normal to the flame front in the measuring plane is $\boldsymbol{n}_{xy}$ with $\boldsymbol{n}_{xy} = \boldsymbol{n}_{xy}(n_{x,xy}, n_{y,xy})$ which could be measured with planar images.

The in-plane angle θ is defined as the angle between $\boldsymbol{n}_{xy}^{p}$ and the axis of y, i.e. $\theta = \arctan 2(n_x, n_y)$, and the out-of-plane angle ϕ is defined as the angle between $\boldsymbol{n}$ and the x–y plane, i.e. $\phi = \arcsin(n_z)$. The angle θ is known from planar measurement and satisfies $-\pi \leqslant \theta \leqslant \pi$, while the angle ϕ is unknown from planar measurement and is in the range of $-\pi/2 \leqslant \phi \leqslant \pi/2$. Based on these notations, it is obvious that the most probable values of (θ, ϕ) should be roughly $(-\pi/2, 0)$ for freely propagating planar flames and $(-\pi$ or $\pi, 0)$ for the slot-jet flame, if we only consider the flame branch with $y > L_y/2$ and neglect the shear layer effect. For an isotropic distribution of a unit vector, the PDFs of θ and ϕ can be written as (Veynante *et al.* 2010*b*; Wang *et al.* 2016)

$$P_\theta(\theta) = 1/2\pi, \tag{3.2}$$

$$P_\phi(\phi) = \cos\phi/2. \tag{3.3}$$

3.2. *The calculation of 2-D and 3-D flame stretch*

The methods for 2-D and 3-D estimations of flame stretch and its related quantities are explained. Equation (1.1) can be recast into

$$\frac{\delta \dot{A}}{\delta A} = (\delta_{ij} - n_i n_j)\frac{\partial \dot{X}_i}{\partial x_j} = a_t + S_d(\boldsymbol{\nabla} \cdot \boldsymbol{n}), \tag{3.4}$$

where a_t is the flame tangential strain rate and $\boldsymbol{\nabla} \cdot \boldsymbol{n}$ is the flame curvature. It is obvious that the flame curvature, tangential strain rate and displacement velocity are key quantities that determine the flame stretch. Therefore, these flame stretch-related quantities will be examined in detailed. The tangential strain rate, a_t, is calculated as

$$a_t = \boldsymbol{\nabla} \cdot \boldsymbol{u} - a_n, \tag{3.5}$$

where $\boldsymbol{\nabla} \cdot \boldsymbol{u}$ is the dilatation and a_n is the normal strain rate calculated as

$$a_n = n_i S_{ij} n_j, \tag{3.6}$$

where S_{ij} is the strain rate tensor component defined as

$$S_{ij} = (\partial u_i/\partial x_j + \partial u_i/\partial x_i)/2. \tag{3.7}$$

The transport equation of the progress variable c is

$$\rho\frac{\mathrm{D}c}{\mathrm{D}t} = \dot{\omega}_c + \frac{\partial}{\partial x_i}\left(\rho D_c \frac{\partial c}{\partial x_i}\right), \tag{3.8}$$

where $\dot{\omega}_c$ is the reaction rate of the progress variable and D_c is the diffusivity of the progress variable. The progress variable isosurface propagates at a speed of S_d, which can be estimated as $S_d = S_a - \boldsymbol{u} \cdot \boldsymbol{n}$ (Poinsot & Veynante 2005), where S_a is the absolute

velocity of the flame. In the practice of DNS, S_d is calculated as (Wang *et al.* 2017*a*,*b*)

$$S_d = \frac{1}{|\nabla c|}\frac{\mathrm{D}c}{\mathrm{D}t} = \frac{\dot{\omega}_c}{\rho|\nabla c|} + \frac{1}{\rho|\nabla c|}\frac{\partial}{\partial x_i}\left(\rho D_c \frac{\partial c}{\partial x_i}\right). \tag{3.9}$$

The 2-D estimation of various quantities in the x–y plane is discussed. The 2-D curvature is denoted as

$$(\nabla \cdot \boldsymbol{n})_{2D} = \frac{\partial n_{x,xy}}{\partial x} + \frac{\partial n_{y,xy}}{\partial y}. \tag{3.10}$$

The 2-D tangential strain rate $a_{t,2D}$ is estimated as

$$a_{t,2D} = (\nabla \cdot \boldsymbol{u})_{2D} - a_{n,2D}, \tag{3.11}$$

where $(\nabla \cdot \boldsymbol{u})_{2D}$ is the 2-D dilatation in the x–y plane computed as

$$(\nabla \cdot \boldsymbol{u})_{2D} = \frac{\partial u}{\partial x} + \frac{\partial v}{\partial y}. \tag{3.12}$$

The quantity $a_{n,2D}$ is the 2-D normal strain rate in the x–y plane with

$$a_{n,2D} = n_{i,xy} S_{ij,xy} n_{j,xy}, \tag{3.13}$$

where $S_{ij,xy}$ is the strain rate tensor component in the x–y plane.

The 2-D displacement velocity $S_{d,2D}$ can be measured experimentally as $S_{d,2D} = S_{a,xy} - \boldsymbol{u}_{xy} \cdot \boldsymbol{n}_{xy}$ (Hartung *et al.* 2009), where $S_{a,xy}$ is the absolute velocity of the flame and $\boldsymbol{u}_{xy}$ is the 2-D flow velocity in the x–y plane. By accounting for the out-of-plane fluid motion, it is estimated in the DNS by the following apparent relationship (Hartung *et al.* 2009; Chakraborty *et al.* 2011; Hawkes *et al.* 2011):

$$S_{d,2D} = S_d / \cos\phi. \tag{3.14}$$

The 2-D flame stretch can be, therefore, computed as $a_{t,2D} + S_{d,2D}(\nabla \cdot \boldsymbol{n})_{2D}$.

3.3. *Statistical tools*

The analysis in this paper employs surface averaged quantities. The fine-grained flame surface density Σ^* is defined as (Veynante & Vervisch 2002)

$$\Sigma^* = \overline{|\nabla c|\delta(c - c^*)}, \tag{3.15}$$

where $|\nabla c|$ is the surface density function and δ is the delta function. The operation $\overline{(\cdot)}$ denotes ensemble average. The fine-grained surface average of a quantity Q is denoted as

$$\langle Q \rangle_s^* = \frac{\overline{Q|\nabla c|\delta(c - c^*)}}{\Sigma^*}. \tag{3.16}$$

The flame stretch and the related quantities are averaged on the isosurface of the progress variable $c = c^*$, so that the results depend on the choice of c^*. The generalized flame surface density Σ has been introduced to overcome this problem (Borger *et al.* 1998;

Veynante & Vervisch 2002; Chakraborty & Cant 2004), which is obtained by integrating (3.15) over all isosurface levels,

$$\Sigma = \int_0^1 \Sigma^* \, \mathrm{d}c^* = \int_0^1 \overline{|\nabla c| \delta(c - c^*)} \, \mathrm{d}c^* = \overline{|\nabla c|}. \tag{3.17}$$

The generalized surface average of Q is denoted as

$$\langle Q \rangle_s = \frac{\overline{Q|\nabla c|}}{\Sigma}. \tag{3.18}$$

Statistics such as PDF and joint PDF are also explored to reveal the difference between 2-D and 3-D flame stretch and the related quantities. Consistent with the generalized surface average, the PDF and joint PDF are also weighted by $|\nabla c|$. In order to exclude regions where reaction is unimportant, the results are conditioned on $0.3 \leqslant c \leqslant 0.9$.

3.4. *Models for converting 2-D to 3-D statistics*

We derive models to convert statistics of a flame stretch-related quantity ψ from 2-D measurements to 3-D reality, assuming isotropy of the flame normal vector orientation. Particularly, the aim is to use the 2-D surface averaged quantity $\langle \psi_{2D} \rangle_s$ to obtain $\langle \psi \rangle_{s,M}$, and to use the 2-D PDF $P_{\psi,2D}(\psi_{2D})$ to obtain $P_{\psi,M}(\psi)$, where the subscript 'M' indicates a specific model.

3.4.1. *Tangential strain rate model*

Following the notations of Hawkes *et al.* (2011), the 3-D tangential strain rate can be written as

$$a_t = \frac{\partial u_{t1}}{\partial x_{t1}} + \frac{\partial u_{t2}}{\partial x_{t2}}, \tag{3.19}$$

where t_1 is tangent to the flame that also lies in the measuring plane and t_2 is the flame tangent perpendicular to t_1. Now the 2-D tangential strain rate in the measuring plane is

$$a_{t1,2D} = \frac{\partial u_{t1}}{\partial x_{t1}} \tag{3.20}$$

while the 2-D out-of-plane tangential strain rate is

$$a_{t2,2D} = \frac{\partial u_{t2}}{\partial x_{t2}}. \tag{3.21}$$

Two assumptions will be developed: the first is that $a_{t1,2D} = a_{t2,2D}$; the second is that $a_{t1,2D}$ and $a_{t2,2D}$ are statistically independent. Both assumptions lead to the following

relationship of 2-D and 3-D surface averaged tangential strain rate:

$$\langle a_t \rangle_{s,M} = 2\langle a_{t,2D} \rangle_s. \tag{3.22}$$

If $a_{t1,2D} = a_{t2,2D}$, the 2-D PDF is related to the 3-D one by

$$P_{a_t,M1}(a_t) = \tfrac{1}{2} P_{a_{t,2D}}\left(\tfrac{1}{2} a_t\right). \tag{3.23}$$

If we assume that $a_{t1,2D}$ and $a_{t2,2D}$ are statistically independent, the PDF of their sum is the convolution of their PDFs,

$$P_{a_t,M2}(a_t) = \int_{-\infty}^{\infty} P_{a_{t1,2D}}(a_{t1}) P_{a_{t2,2D}}(a_t - a_{t1})\, \mathrm{d}a_{t1}. \tag{3.24}$$

Because of isotropy, the statistics of a_{t1} and a_{t2} are identical, i.e. $P_{a_{t1,2D}} = P_{a_{t2,2D}}$, so that

$$P_{a_t,M2}(a_t) = \int_{-\infty}^{\infty} P_{a_{t1,2D}}(a_{t1}) P_{a_{t1,2D}}(a_t - a_{t1})\, \mathrm{d}a_{t1}. \tag{3.25}$$

3.4.2. *Curvature model*

From Hawkes *et al.* (2011), the curvature measured in 2-D is related to the 3-D principal curvatures by

$$\cos\phi\, (\boldsymbol{\nabla} \cdot \boldsymbol{n})_{2D} = \kappa_1 \cos^2\alpha + \kappa_2 \sin^2\alpha, \tag{3.26}$$

where κ_1 and κ_2 are the two principal curvatures with the corresponding principal vectors denoted as $\boldsymbol{k}_1$ and $\boldsymbol{k}_2$, respectively. The unit vector $\boldsymbol{t}_1$ is lying in both the measuring plane and the flame tangent plane. Here α is the angle between $\boldsymbol{t}_1$ and $\boldsymbol{k}_1$. Note that the above relationship is general and no assumptions are made (Hawkes *et al.* 2011). If ϕ and α are not correlated with other variables, the following is obtained:

$$\langle \cos\phi \rangle_s \, \langle (\boldsymbol{\nabla} \cdot \boldsymbol{n})_{2D} \rangle_s = \langle \kappa_1 \rangle_s \langle \cos^2\alpha \rangle_s + \langle \kappa_2 \rangle_s \langle \sin^2\alpha \rangle_s. \tag{3.27}$$

By assuming ϕ and α are isotropically distributed, we have $\langle \cos\phi \rangle_s = \pi/4$ and $\langle \cos^2\alpha \rangle_s = \langle \sin^2\alpha \rangle_s = 1/2$. Finally, the following surprisingly simple relationship is obtained:

$$\langle (\boldsymbol{\nabla} \cdot \boldsymbol{n})_{2D} \rangle_s = \pi/2 (\langle \kappa_1 \rangle_s + \langle \kappa_2 \rangle_s) = 2/\pi \, \langle \boldsymbol{\nabla} \cdot \boldsymbol{n} \rangle_s \,, \tag{3.28}$$

where $\boldsymbol{\nabla} \cdot \boldsymbol{n} = \kappa_1 + \kappa_2$ is the 3-D curvature. So that the surface averaged $\boldsymbol{\nabla} \cdot \boldsymbol{n}$ can be modelled as

$$\langle \boldsymbol{\nabla} \cdot \boldsymbol{n} \rangle_{s,M} = \pi/2 \, \langle (\boldsymbol{\nabla} \cdot \boldsymbol{n})_{2D} \rangle_s \,. \tag{3.29}$$

The following model is proposed to approximately the PDF of $\boldsymbol{\nabla} \cdot \boldsymbol{n}$, using that of $(\boldsymbol{\nabla} \cdot \boldsymbol{n})_{2D}$:

$$P_{\boldsymbol{\nabla}\cdot\boldsymbol{n},M}(\boldsymbol{\nabla} \cdot \boldsymbol{n}) = \frac{2}{\pi} P_{(\boldsymbol{\nabla}\cdot\boldsymbol{n})_{2D}}\left(\frac{2}{\pi} \boldsymbol{\nabla} \cdot \boldsymbol{n}\right). \tag{3.30}$$

3.4.3. *Displacement velocity model*

If we assume S_d and ϕ are not correlated and using (3.14), the surface averaged S_d are modelled, using that of $S_{d,2D}$, by

$$\langle S_d \rangle_{s,M} = \langle S_{d,2D} \rangle_s \langle \cos\phi \rangle_s = \pi/4 \langle S_{d,2D} \rangle_s. \tag{3.31}$$

The following model is proposed to connect the PDF of S_d and that of $S_{d,2D}$:

$$P_{S_d,M}(S_d) = \frac{4}{\pi} P_{S_{d,2D}}\left(\frac{4}{\pi} S_d\right). \tag{3.32}$$

4. Results and discussion

In this section, the general characteristics of various flames are first discussed and the flame normal vector orientations are quantified. Then, the instantaneous and statistical flame stretch-related quantities are explored, and the 2-D and 3-D results are compared. Models for approximating the 3-D results using the 2-D measurements are evaluated. Third, the instantaneous and statistical results of 2-D and 3-D flame stretch are compared and discussed. Finally, the 2-D and 3-D turbulence–flame interactions are examined for various DNS cases, and the discrepancy of turbulence–flame interactions from 2-D and 3-D measurements are highlighted.

4.1. *General characteristics*

The general characteristics of the DNS cases are discussed. Figure 1(*a*) shows the isosurface of vorticity magnitude coloured by the progress variable and the isosurface of $c = 0.8$ coloured by HRR for freely propagating planar flames. Note that $c = 0.8$ corresponds to the location of maximum HRR in the corresponding laminar flame. Fine-scale eddies are observed in the reactants and the eddies become fewer and larger behind the flame front, which is due to the thermal expansion effects (Tanahashi, Fujimura & Miyauchi 2000). The intensity of turbulent eddies is increased from case *L* to case *H*. For case *M* and case *H* in the broken reaction zones regime, the fine-scale eddies are able to enter into the reaction zone so that the inner flame structures are affected. The distributions of surface density function, $|\nabla c|$, are also shown for freely propagating planar flames. The surface density function can be regarded as a reciprocal flame thickness (Wang *et al.* 2017*b*). Moreover, it is closely related to the flame surface density as seen in the previous section. Figure 1(*a*) indicates that with increasing *Ka*, the fluctuation of $|\nabla c|$ becomes more evident. Local thinning of the flame front in case *H* is clearly observed. But on average the flame brush is thicker in case *H* compared with the other two cases. Similar observations were made in a premixed jet flame by Wang *et al.* (2017*b*).

Figure 1(*b*) displays 3-D rendering of the progress variable and the isosurface of $c = 0.8$ coloured by HRR for the slot-jet flame. As can be seen, the HRR is negligible in the near field, where only mixing of the jet and coflow occurs. Evident HRR is observed after $x/H = 5$ when autoignition occurs. The magnitude of HRR increases with increasing downstream distance. Wang *et al.* (2017*a*) showed that such enhanced reaction rate in jet-type flames is related to enhanced levels of radicals such as OH and H in the downstream region. There are significant interactions between the shear-generated turbulence and the flame, modifying the flame topology, as will be quantified shortly.

Figure 1 indicates that both the freely propagating planar and slot-jet flames exhibit evident 3-D behaviours. Therefore, the flame orientations are analysed. For the slot-jet

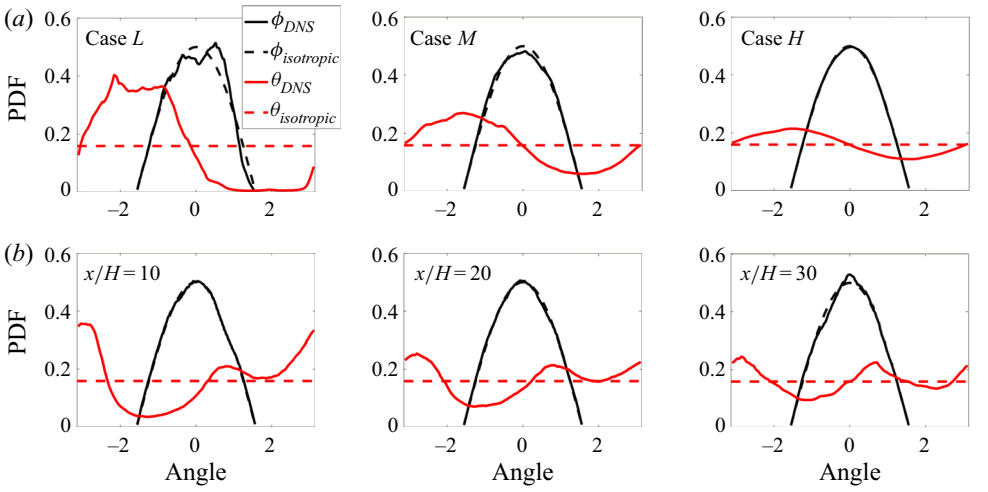

Figure 3. The PDFs of the out-of-plane angle ϕ and the in-plane-angle θ for the (*a*) freely propagating planar flames and (*b*) slot-jet flame.

flame, three downstream locations, i.e. $x/H = 10$, 20 and 30, are selected for the analysis. Figure 3 shows the PDFs of the out-of-plane angle ϕ and the in-plane angle θ for various cases. As can be seen, the distribution of ϕ is very similar to that predicted using (3.3), implying that the distribution of ϕ is close to isotropy. This is valid for both flames with and without a mean shear. For freely propagating planar flames, the most probable value of θ is approximately $-\pi/2$, as expected. The distribution of θ becomes more isotropic with increasing *Ka*, due to the influence of intense turbulence. This observation is consistent with previous experimental results (Lee *et al.* 1992). A different picture is observed for the slot-jet flame. In particular, the most probable value of θ is approximately $-3\pi/4$ or $\pi/4$. This is attributed to the local flame surface convex towards the products due to the presence of mean shear (Wang *et al.* 2016). Particularly, as will be shown later, the flame normal vector aligns with the most compressive strain rate of the flow, which roughly orients roughly $-3\pi/4$ or $\pi/4$ to the radial direction. The results are also consistent with previous studies of passive scalars in non-reacting shear flows (Ashurst *et al.* 1987; Nomura & Elghobashi 1992). The distribution of θ is more isotropic with increasing downstream distance for the slot-jet flame.

The joint PDFs of out-of-plane angle ϕ and the in-plane angle θ for various cases are shown in figure 4. For both the freely propagating planar and slot-jet flames, the two angles are poorly correlated. Similar results were reported by Veynante *et al.* (2010*b*) and Wang *et al.* (2016). Consequently, the joint PDF of ϕ and θ could be modelled using the product of their marginal PDFs, i.e. $P_{\phi\theta}(\phi, \theta) = P_{\phi}(\phi)P_{\theta}(\theta)$.

The correlation of ϕ and θ is further demonstrated using the independence function, which is defined as $I(\phi, \theta) = P_{\phi\theta}(\phi, \theta)/P_{\phi}(\phi)/P_{\theta}(\theta)$. Unity values of the independence function indicate that ϕ and θ are independent. Figure 5 shows the values of I in various cases. As can be seen, I is close to unity in most regions. There are also regions where I is much larger or smaller than unity, the PDF of which is, however, small as seen in figure 4.

4.2. *Evaluation of the models for flame stretch-related quantities*

The orientations of the out-of-plane angle ϕ and the in-plane angel θ examined above play significant roles in the relationship between 2-D and 3-D values of flame

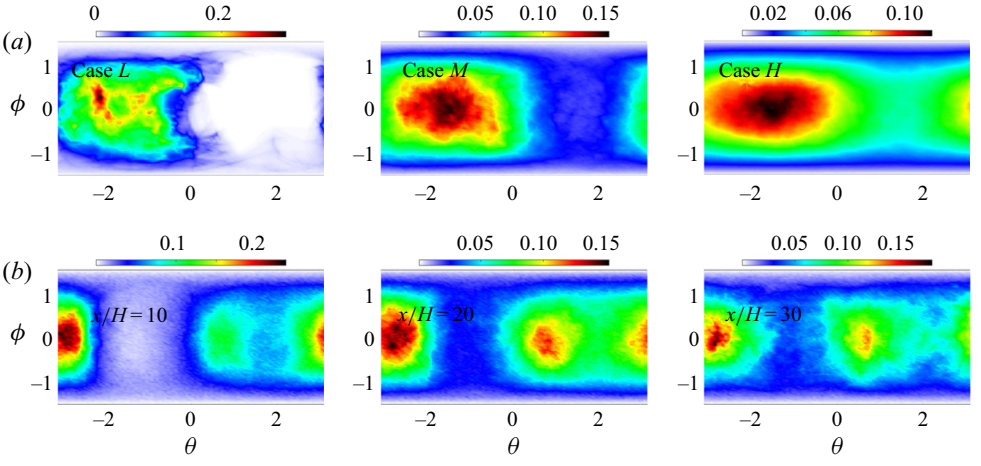

Figure 4. Joint PDFs of out-of-plane angle ϕ and the in-plane angle θ for the (a) freely propagating planar flames and (b) slot-jet flame.

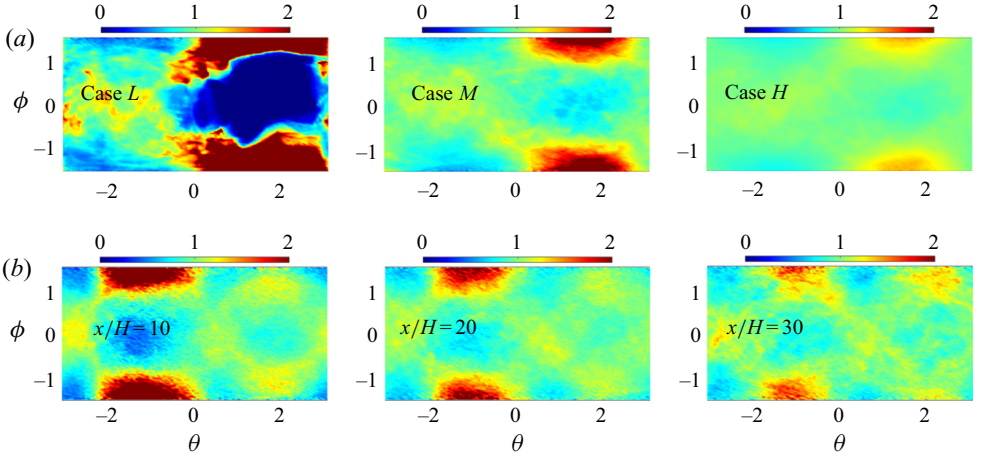

Figure 5. Independence functions of out-of-plane angle ϕ and the in-plane angle θ for the (a) freely propagating planar flames and (b) slot-jet flame.

stretch-related quantities. The assumption of ϕ being isotropic has also been employed to derive models that convert 2-D to 3-D statistics of flame properties, as demonstrated in § 3.4. Let us now consider the flame stretch-related quantities, i.e. tangential strain rate, curvature and displacement velocity. Figure 6 shows the instantaneous 2-D and 3-D values of these quantities along $c = 0.8$ from a typical x–y plane of case M. As can be seen, the flame front is wrinkled by turbulence. Very large positive curvature is observed in both 2-D and 3-D results, which corresponds to small-scale wrinkling of the flame front. In general, the 3-D values of curvature are higher than the 2-D values along the flame. The 3-D tangential strain rate is also larger than the 2-D one. In contrast, the 3-D displacement velocity is slightly smaller than the 2-D one, as expected from (3.14). It is interesting to see that there is a negative correlation between the displacement velocity and curvature, consistent with Wang *et al.* (2017*a*) for methane–air premixed jet flames.

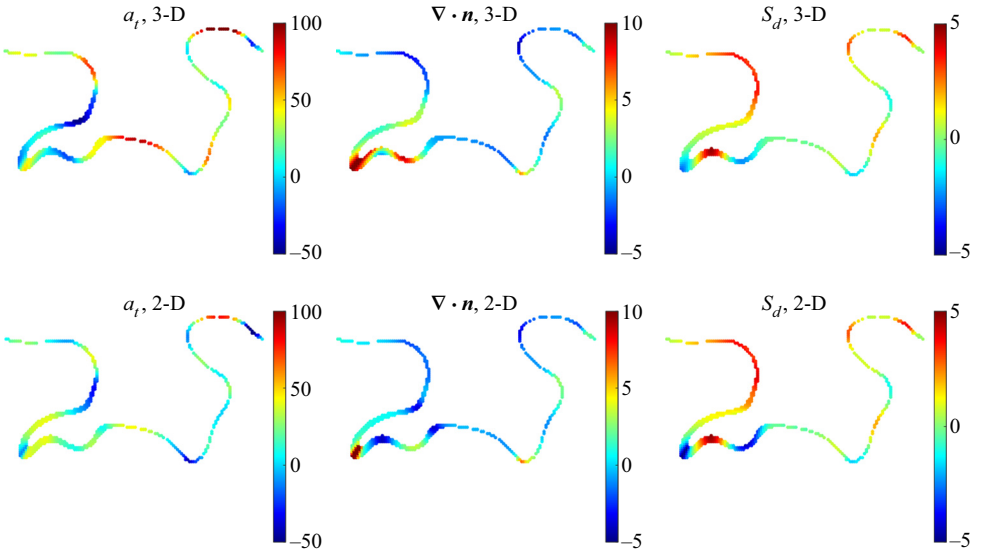

Figure 6. Comparison of instantaneous 2-D and 3-D values of tangential strain rate $a_t\tau_L$, curvature $(\nabla \cdot \boldsymbol{n})\delta_L$ and displacement velocity S_d/S_l along $c = 0.8$ from a typical slice of case M.

More difference between the 2-D and 3-D values of flame stretch-related quantities is shown, and the performance of models described in § 3.4 is evaluated. Figure 7 compares 2-D, 3-D and model predicted surface averaged tangential strain rate, curvature and displacement velocity for various cases. For freely propagating planar flames, the results are shown across the flame brush as a function of the Favre averaged progress variable $\tilde{c}$, while for the slot-jet flame, the results along the streamwise direction are presented. As can be seen, the 3-D surface averaged tangential strain rate and curvature are generally larger than their 2-D counterparts, while the 3-D surface averaged displacement velocity is smaller than the 2-D result in magnitude. The model predictions are in overall good agreement with the actual 3-D surface averaged quantities for various cases.

It is crucial to predict accurately the PDFs for flame stretch-related quantities. Figure 8 shows the 2-D, 3-D and model predicted PDFs of the tangential strain rate for various cases. Three representative axial locations of case J are selected for the analysis. The model based on (3.23) is labelled as 'M1' and that based on (3.24) is labelled as 'M2'. Several observations can be made. First, the range of tangential strain rate is broadened with increasing Ka in freely propagating planer flames, which is due to the large straining induced in highly turbulent flames. Second, the tangential strain rate in the slot-jet flame is decreased with downstream distance, in line with the decaying of the jet. Third, the prediction of M2 is in excellent agreement with the actual 3-D PDF, although the peak is over predicted at $x/H = 10$ of case J. Comparatively, the prediction of M1 is less accurate than M2.

To provide quantitative measures of the performance of the modelled PDFs, a Kullack–Leibler divergence is introduced (Kullback & Leibler 1951). The Kullack–Leibler divergence from the actual 3-D PDF, P_{a_t}, to the modelled 3-D PDF, $P_{a_t,M}$, is defined as

$$D_{KL} = \sum_{x\in X} P_{a_t}(x) \log\left(\frac{P_{a_t}(x)}{P_{a_t,M}(x)}\right), \tag{4.1}$$

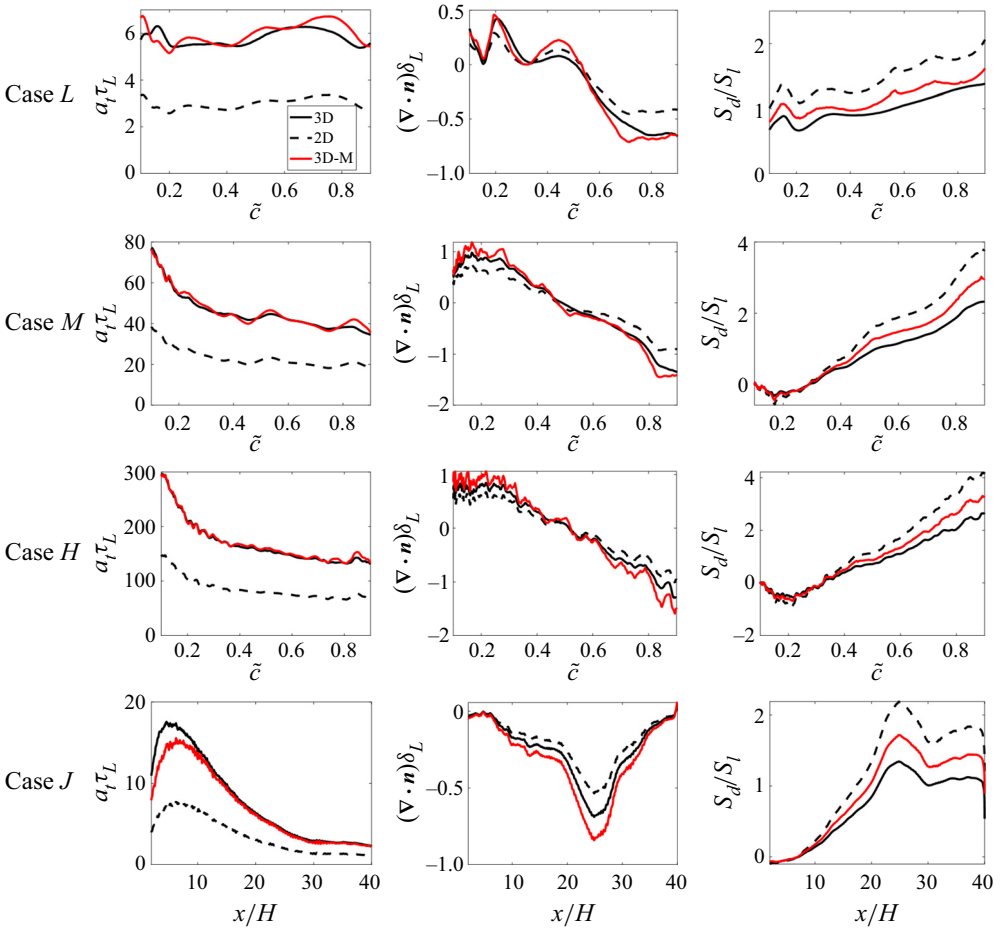

Figure 7. Comparison of 2-D, 3-D and model predicted surface averaged tangential strain rate $a_t\tau_L$, curvature $(\nabla\cdot\boldsymbol{n})\delta_L$ and displacement velocity S_d/S_l across the flame brush of case *L*, case *M* and case *H* and along the streamwise direction of case *J*.

where X is the probability space of the tangential strain rate. The Kullack–Leibler divergence measures how one PDF is different from a second. A zero value of D_{KL} indicates that the two PDFs are identical. The results of the Kullack–Leibler divergence for various cases are shown in figure 9. It is observed that the values of D_{KL} for M2 are lower than those for M1 in all cases, which confirms that M2 is more accurate than M1.

The PDFs of curvature are compared in figure 10. For reference, the curvature measured in the y–z plane is also displayed. It can be seen that the curvature PDFs from the x–y plane and the y–z plane almost overlap in various cases. Some minor difference is observed in case *L*, where the peak value of the curvature PDF in the x–y plane is larger than that in the y–z plane. The 3-D curvature distributions are wider than their 2-D counterparts. The model based on (3.30) is performing reasonably well in all cases.

Finally, the 2-D, 3-D and modelled PDFs of displacement velocity are compared in figure 11. Negative displacement velocity is observed in various cases, which has been reported in previous DNS studies (Chakraborty *et al.* 2011; Sankaran *et al.* 2015; Wang *et al.* 2017*a*). The range of displacement velocity is broadened as turbulent intensity

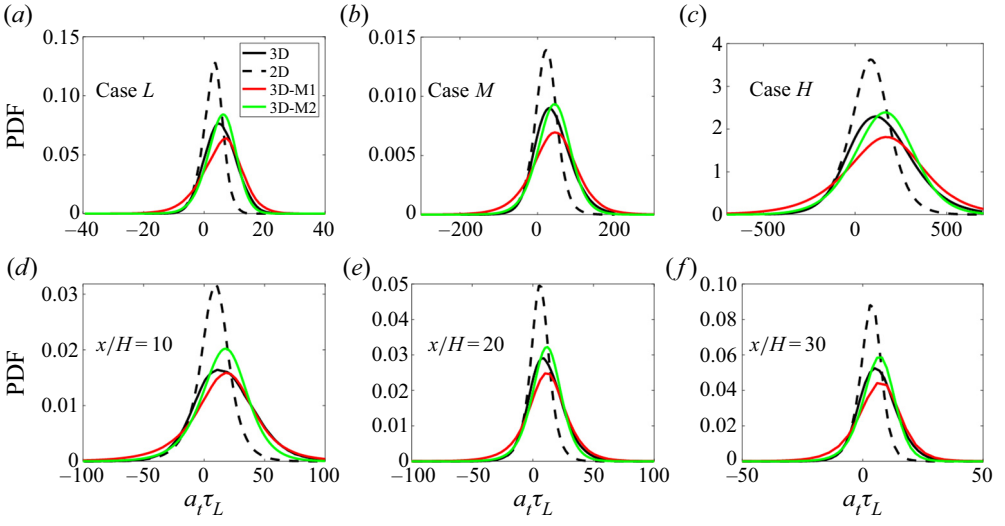

Figure 8. Comparison of 2-D, 3-D and model predicted PDFs of tangential strain rate for various cases.

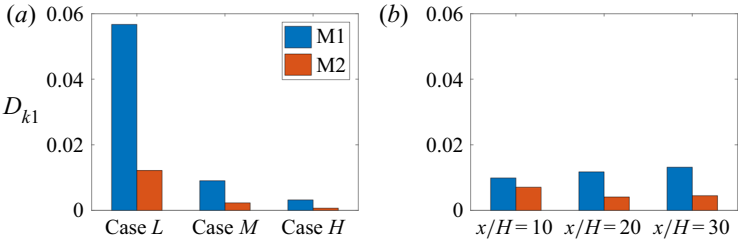

Figure 9. Results of the Kullack–Leibler divergence for the tangential strain rate with different 3-D PDF models in the (*a*) freely propagating planar flames and (*b*) slot-jet flame.

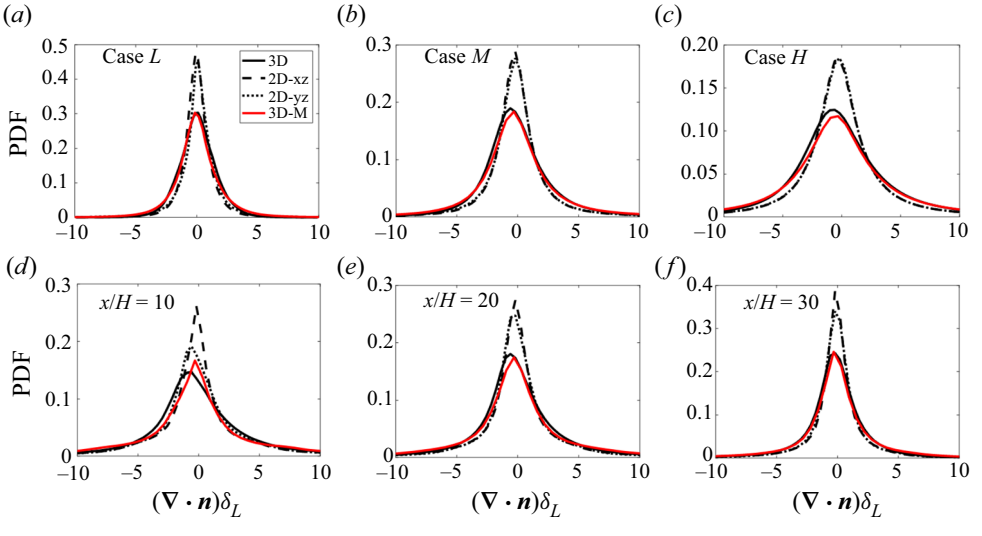

Figure 10. Comparison of 2-D, 3-D and model predicted PDFs of curvature for various cases.

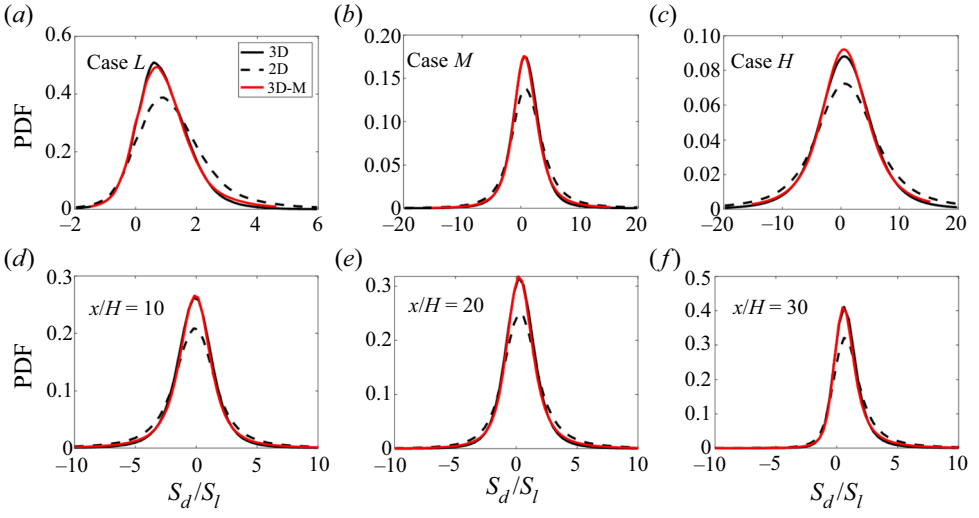

Figure 11. Comparison of 2-D, 3-D and model predicted PDFs of displacement velocity for various cases.

increases in freely propagating planer flames. As can be seen, the model prediction based on (3.32) is in very good agreement with the actual 3-D PDF for all cases.

4.3. *Flame stretch*

In this section, the 2-D and 3-D flame stretch results are presented. Figure 12 shows the instantaneous 2-D and 3-D values of flame curvature, tangential strain rate, curvature stretch and total flame stretch along $c = 0.8$ from a typical x–y plane of case M. Note that flame stretch consists of tangential strain rate and curvature stretch. It has been shown previously that tangential strain rate tends to produce flame surface area while curvature stretch tends to destroy it (Candel & Poinsot 1990; Wang *et al.* 2017*b*; Luca *et al.* 2019). This is also true for the current DNS flames. Figure 12 indicates that the mean tangential strain rate is positive and the mean curvature stretch is negative. In general, the 2-D flame stretch and its components are smaller than their 3-D counterparts.

There is evident correlation between flame stretch and curvature as shown in figure 12. In order to further assess the correlation, the joint PDFs of flame stretch and curvature for freely propagating planar flames are shown in figure 13. Both the 2-D and 3-D results are displayed. It is clearly observed that the flame stretch is positive in regions with low curvature magnitudes, and highly negative flame stretch occurs in regions with large curvature, the sign of the curvature being unimportant. It is, therefore, concluded that flame area tends to be produced in low curvature regions while it is destroyed in high curvature regions. This is consistent with the results reported in (Wang *et al.* 2017*b*). With increasing levels of turbulence from case L to case H, the magnitude of flame stretch also increases. It is interesting to see that although the magnitudes of flame stretch and curvature are smaller in the 2-D results, the trends of the relationship between flame stretch and curvature are reasonably captured. That is, flame stretch is positive (negative) in low (high) curvature regions.

The joint PDFs of flame stretch and curvature at three locations of the slot-jet flame are shown in figure 14. The existence of mean shear does not alter the correlations between flame stretch and curvature qualitatively. More specifically, the observations made above

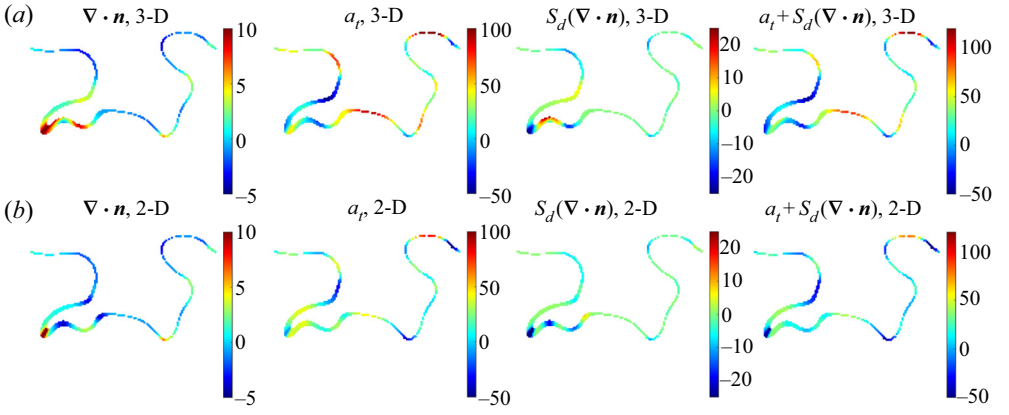

Figure 12. Comparison of instantaneous 2-D and 3-D values of curvature $(\nabla \cdot \boldsymbol{n})\delta_L$, tangential strain rate $a_t\tau_L$ and curvature stretch $S_d(\nabla \cdot \boldsymbol{n})\tau_L$ and total flame stretch $a_t\tau_L + S_d(\nabla \cdot \boldsymbol{n})\tau_L$ along $c = 0.8$ from a typical slice of case M.

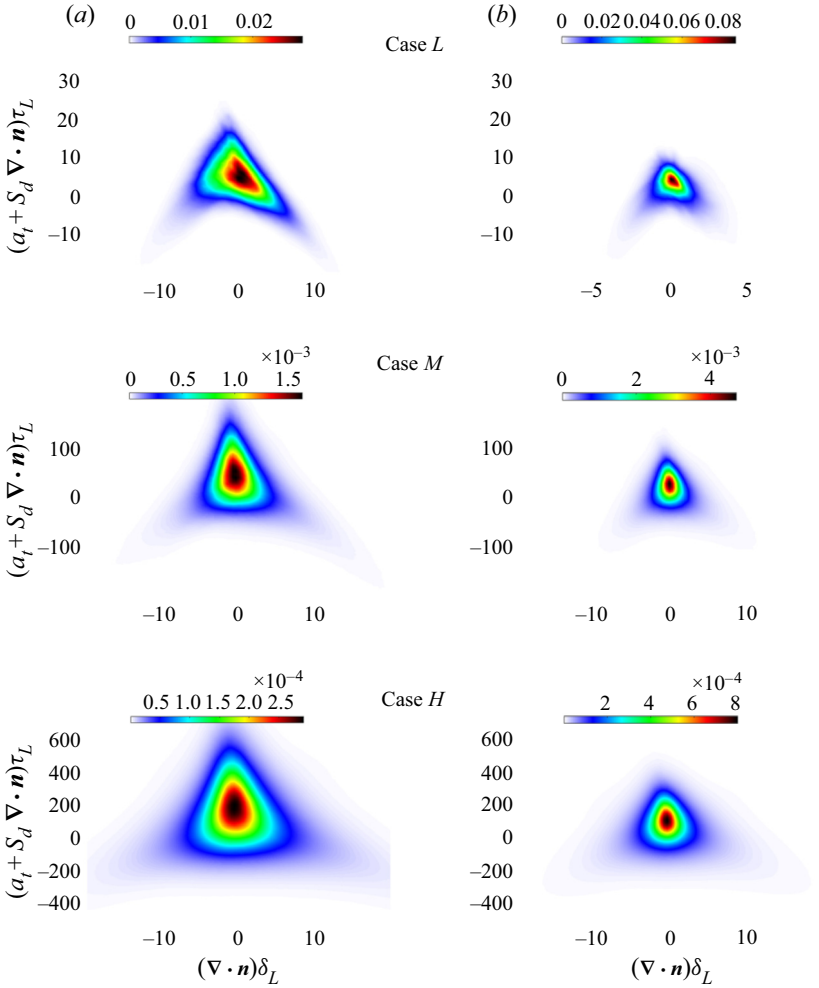

Figure 13. Joint PDFs of (*a*) 3-D and (*b*) 2-D flame stretch and curvature for case L, case M and case H.

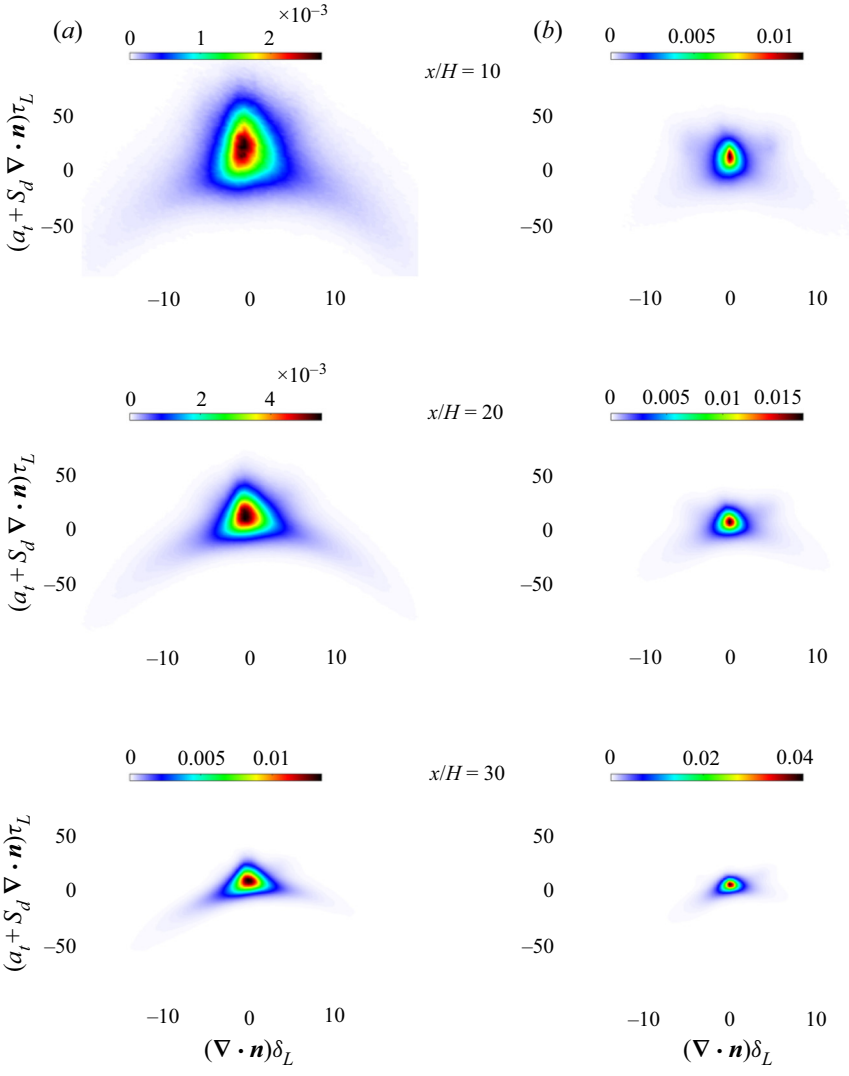

Figure 14. Joint PDFs of (*a*) 3-D and (*b*) 2-D flame stretch and curvature for various locations of case *J*.

for freely propagating planar flames are also valid for the slot-jet flame. The flame stretch generally decreases with downstream distance, until the reactant is consumed completely and the flame disappears.

4.4. *Turbulence–flame interactions*

The turbulence–flame interactions are examined in terms of the flame normal strain rate a_n and its related terms. Both the 2-D and 3-D results are presented. The flame normal strain rate is also written as $n_i S_{ij} n_j$, which was used in the calculation of tangential strain rate (3.5) and flame stretch. According to Wang *et al.* (2016), a_n can be recast as

$$a_n = n_i S_{ij} n_j = \lambda_1 |\boldsymbol{n} \cdot \boldsymbol{e}_1|^2 + \lambda_2 |\boldsymbol{n} \cdot \boldsymbol{e}_2|^2 + \lambda_3 |\boldsymbol{n} \cdot \boldsymbol{e}_3|^2, \tag{4.2}$$

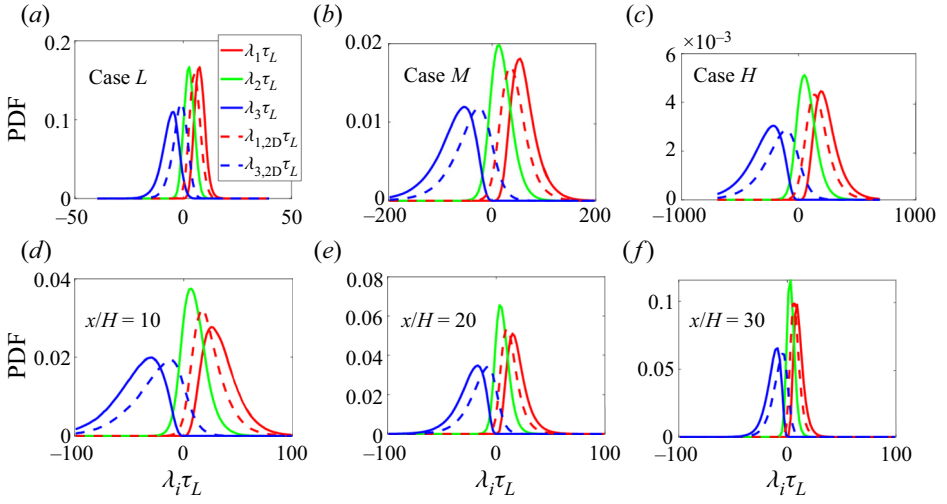

Figure 15. The 2-D and 3-D PDFs of principal strain rates for various cases.

where λ_1, λ_2 and λ_3 are the three principal eigenvalues of the velocity gradient tensor $\partial u_i/\partial x_j$ by the convention $\lambda_1 \geqslant \lambda_2 \geqslant \lambda_3$, which are determined from the characteristic equation of $\partial u_i/\partial x_j$ as follows:

$$\lambda^3 + P\lambda^2 + Q\lambda + R = 0 \tag{4.3}$$

with the invariants specified as $P = -S_{ii}$, $Q = (P^2 - S_{ij}S_{ji} - W_{ij}W_{ji})/2$ and $R = (-P^3 + 3PQ - S_{ij}S_{jk}S_{ki} - 3W_{ij}W_{jk}S_{ki})/3$, where $W_{ij} = (\partial u_i/\partial x_j - \partial u_j/\partial x_i)/2$ is the rotation tensor.

The eigenvectors of λ_1, λ_2 and λ_3 are $\boldsymbol{e}_1$, $\boldsymbol{e}_2$ and $\boldsymbol{e}_3$, respectively. The orientations of the flame normal vector relative to the principal strain rate directions are characterized by the absolute value of the cosine of the angle between the flame normal vector and the strain rate eigenvectors, i.e. $|\boldsymbol{n} \cdot \boldsymbol{e}_i|$. Note that in 2-D measurements, only the most extensive strain rate $\lambda_{1,xy}$ and the most compressive strain rate $\lambda_{3,xy}$ are available, while the intermediate strain rate $\lambda_{2,xy}$ is absent. Accordingly, only $|\boldsymbol{n}_{xy} \cdot \boldsymbol{e}_{1,xy}|$ and $|\boldsymbol{n}_{xy} \cdot \boldsymbol{e}_{3,xy}|$ are evaluated for the alignment between the flame normal vector and principal strain rates, while $|\boldsymbol{n}_{xy} \cdot \boldsymbol{e}_{2,xy}|$ is not available.

Figure 15 shows the PDFs of the principal strain rates for various cases. As can be seen, the most extensive strain rate of the 3-D results is always positive while the most compressive strain rate is negative. The most probable value of the intermediate strain rate is close to zero, and its distribution is positively skewed. The magnitude of the principal strain rates increases with *Ka* for freely propagating planar flames and decreases with downstream distance for the slot-jet flame, as expected. The principal strain rates of 2-D measurements are also shown. The profiles of $\lambda_{1,xy}$ and $\lambda_{3,xy}$ are very similar to those of λ_1 and λ_3. However, the most extensive (compressive) strain rate of 2-D measurements can be negative (positive). It is concluded that the above behaviours of the 2-D and 3-D principal strain rates are valid in flames with and without a mean shear. The distributions of the 2-D principal strain rates have been measured experimentally by Hartung *et al.* (2008) in premixed ethylene–air flames stabilized on a bluff body, and qualitatively similar PDFs of the 2-D principal strain rates were reported (see Hartung *et al.* (2008), figure 10).

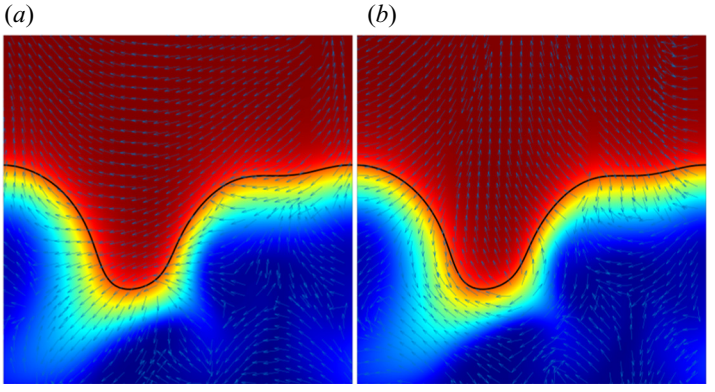

Figure 16. Distributions of the progress variable in a typical slice of case *L*: (*a*) the arrows show the eigenvector of the 2-D most extensive strain rate and (*b*) the arrows show the eigenvector of the 2-D most compressive strain rate. The black line shows the isoline of $c = 0.8$.

The orientation between the flame normal vector and the principal strain rate determines whether the scalar gradient $|\nabla c|$ are produced or destroyed by turbulence (Chakraborty & Swaminathan 2007; Kim & Pitsch 2007; Sponfeldner *et al.* 2015; Wang *et al.* 2016). Previous investigations of turbulence–scalar interaction in non-reacting flows with and without a mean shear showed a preferential alignment of scalar gradient vector with the most compressive principal strain rate (Ashurst *et al.* 1987). The effects of chemical reactions on the alignment characteristics have been studied in (Swaminathan & Grout 2006; Chakraborty & Swaminathan 2007; Kim & Pitsch 2007; Cifuentes *et al.* 2014), where it was found that the scalar gradient aligns with the most extensive strain rate and turbulence dissipates the scalar gradient in high *Da* flames. This is because in high *Da* flames the dilatation induced by heat release is dominant over the turbulent strain rate. The turbulence–flame interactions of high *Ka* flames were investigated by Wang *et al.* (2016) and it was concluded that consistent with non-reacting flows, the scalar gradient aligns with the most compressive strain rate and turbulence generates the scalar gradient. In the present work, the alignment behaviours of the flame normal vector and the principal strain rates are examined in both 2-D and 3-D measurements. Figure 16 shows the distributions of the progress variable in a typical slice of case *L*, which is superimposed with the eigenvector of the most extensive and compressive strain rate of 2-D measurements, i.e. $\boldsymbol{e}_{1,xy}$ and $\boldsymbol{e}_{3,xy}$. There is a clear preferential alignment between $\boldsymbol{e}_{3,xy}$ and $\boldsymbol{n}_{xy}$, while the alignment characteristics between $\boldsymbol{e}_{1,xy}$ and $\boldsymbol{n}_{xy}$ are less obvious. This observation is further quantified below.

The PDFs of $|\boldsymbol{n}\cdot\boldsymbol{e}_i|$ and $|\boldsymbol{n}_{xy}\cdot\boldsymbol{e}_{i,xy}|$ for case *L* are shown in figure 17. The PDFs for other cases have also been extracted and they are very similar to those of case *L*, so that only the results of case *L* are presented. In the 3-D statistics, the flame normal vector aligns preferentially with the most compressive strain rate and misaligns with the most extensive and intermediate strain rates, which is the general feature of high *Ka* (low *Da*) flames (Wang *et al.* 2016). In the 2-D statistics, the alignment of the flame normal vector and the most compressive strain rate is much stronger than its 3-D counterpart. Interestingly, the most probable value of $|\boldsymbol{n}_{xy}\cdot\boldsymbol{e}_{1,xy}|$ is unity in 2-D measurements, while that of $|\boldsymbol{n}\cdot\boldsymbol{e}_1|$ is zero in 3-D measurements.

These findings highlight the difference in 2-D and 3-D measurements of turbulence–flame interactions. Particularly, the flame normal vector is aligned with the

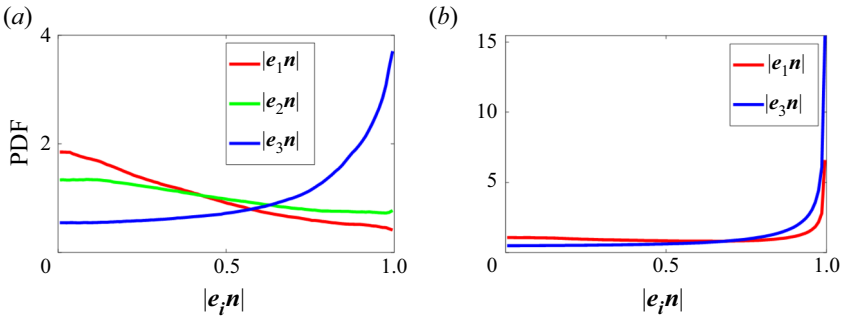

Figure 17. (*a*) The alignment of the 3-D eigenvectors and flame normal and (*b*) the alignment of the 2-D eigenvectors and flame normal for case *L*.

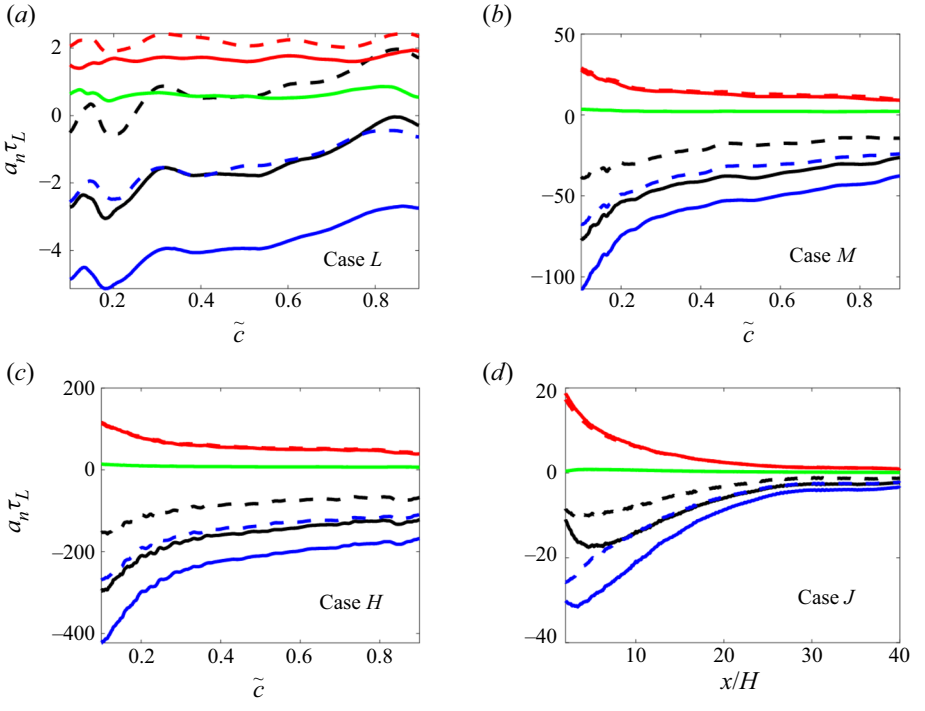

Figure 18. The (dashed lines) 2-D and (solid lines) 3-D surface averaged normal strain rate and its components across the flame brush of case *L*, case *M* and case *H* and along the streamwise direction of case *J*: (black) a_n; red, $\lambda_1|\boldsymbol{e}_1 \cdot \boldsymbol{n}|^2$; green $\lambda_2|\boldsymbol{e}_2 \cdot \boldsymbol{n}|^2$; blue $\lambda_3|\boldsymbol{e}_3 \cdot \boldsymbol{n}|^2$.

most compressive strain rate in both 2-D and 3-D measurements. However, the level of alignment is over-predicted in 2-D measurements. Moreover, the flame normal vector is weakly aligned with the most extensive strain rate in 2-D measurements, however, it is misaligned with the most extensive strain rate in 3-D measurements. This implies the planar measuring results from experiments should be carefully interpreted, as there can be a qualitative difference between the 2-D and 3-D statistics of turbulence–flame interactions.

Finally, the surfaced averaged normal strain rate and its components in (4.2) are evaluated across the flame brush for freely propagating planar flames and along the

streamwise direction for the slot-jet flame in figure 18. Both 2-D and 3-D results are presented. In 3-D statistics of various cases, $\langle a_n \rangle_s$ is always negative. Its magnitude generally decreases across the flame brush for case L, case M and case H, and along the streamwise direction for case J. This is also true for 2-D statistics of most cases. However, in 2-D statistics of case L, $\langle a_{n,xy} \rangle_s$ is largely positive. As the flame normal vector $\boldsymbol{n}$ preferentially aligns with the most compressive strain rate, and λ_3 is negative as shown in figure 15, it is expected that $\lambda_3 |\boldsymbol{e}_3 \cdot \boldsymbol{n}|^2$ is a dominant term for a_n. Indeed, the component breakdown reveals that, in 3-D statistics, the component $\lambda_3 |\boldsymbol{e}_3 \cdot \boldsymbol{n}|^2$ is dominant and negative, while the components $\lambda_1 |\boldsymbol{e}_1 \cdot \boldsymbol{n}|^2$ and $\lambda_2 |\boldsymbol{e}_2 \cdot \boldsymbol{n}|^2$ are small and positive. In 2-D statistics, $\lambda_3 |\boldsymbol{e}_3 \cdot \boldsymbol{n}|^2$ is still dominant in most cases. However, in case L, $\lambda_1 |\boldsymbol{e}_1 \cdot \boldsymbol{n}|^2$ becomes more important, which explains the observed behaviour of positive $\langle a_{n,xy} \rangle_s$ of case L.

5. Conclusions

Flame stretch is a quantity measuring the rate of change of flame surface area, and by nature is 3-D. Most of the current experimental studies can only have access to information of flame stretch and turbulence–flame interactions using planar measurements. Therefore, it is crucial to understand the relationship between 2-D and 3-D flame stretch and propose models that could reconstruct 3-D properties based on 2-D measurements. In this paper, various DNS were performed, including three freely propagating planar flames with various Ka, and a slot-jet flame with a strong mean shear. The DNS data were analysed to provide detailed information of 2-D and 3-D stretch and turbulence–flame interactions.

Turbulent flame orientations exhibit significant 3-D behaviours. In all flame cases, the distribution of the out-of-plane angle is isotropic. The most probable value of the in-plane angle is consistent with the mean flame propagation direction in freely propagating planar flames. It was interesting to see that local peaks of the PDF of the in-plane angle appear near $-3\pi/4$ and $\pi/4$ for the slot-jet flame, which is due to the effects of mean shear. Similar observations have previously been made for passive scalars in non-reacting shear flows. The out-of-plane and in-plane angles are rarely correlated.

The surface averages and PDFs of flame stretch-related quantities, including the flame tangential strain rate, curvature and displacement velocity, were examined, and models were proposed to approximate the 3-D statistics using 2-D measurements. Despite several assumptions being employed in the model development, the modelled 3-D statistics agree well with the actual 3-D statistics of various quantities.

The statistical results of 2-D and 3-D flame stretch were presented. There was evident correlation between flame stretch and curvature. Particularly, flame surface area was generated in low curvature regions while it was destroyed in highly curved regions. This trend was reasonably captured by 2-D measurements, although the magnitude of flame stretch was underestimated.

The 2-D and 3-D turbulence–flame interactions were examined. The profiles of the most extensive and compressive strain rates are qualitatively similar between the 2-D and 3-D results for flames with and without a mean shear. The flame normal vector is aligned with the most compressive strain rate in both 2-D and 3-D measurements. However, the level of alignment was over-estimated in 2-D measurements. The flame normal vector was weakly aligned with the most extensive strain rate in 2-D measurements. But it was misaligned with the most extensive strain rate in 3-D measurements. Therefore, the planar measuring

results of turbulence–flame interactions should be carefully interpreted, as qualitative different trends between the 2-D and 3-D results can exist.

The results are encouraging in that, despite that the mean shear influences the flame orientations, it does not change the flame stretch statistics and turbulence–flame interactions qualitatively. Meanwhile, models were successfully used to correct 2-D measurements and reconstruct 3-D statistics that are relevant to flame stretch. These models will be applied to experimental studies in future work.

Funding. This work was supported by Natural Science Foundation of China (grant nos. 51976185, 91841302).

Declaration of interests. The authors report no conflict of interest.

Author ORCIDs.
Haiou Wang https://orcid.org/0000-0002-6480-2657;
Jianren Fan https://orcid.org/0000-0002-6332-6441.

References

Anselmo-Filho, P., Hochgreb, S., Barlow, R.S. & Cant, R.S. 2009 Experimental measurements of geometric properties of turbulent stratified flames. *Proc. Combust. Inst.* **32** (2), 1763–1770.

Ashurst, W.T., Kerstein, A.R., Kerr, R.M. & Gibson, C.H. 1987 Alignment of vorticity and scalar gradient with strain rate in simulated Navier–Stokes turbulence. *Phys. Fluids* **30**, 2343–2353.

Borger, M., Veynante, D., Boughanem, H. & Trové, A. 1998 Direct numerical simulation analysis of flame surface density concept for large eddy simulation of turbulent premixed combus. *Proc. Combust. Inst.* **27**, 917–925.

Candel, S. & Poinsot, T.J. 1990 Flame stretch and the balance equation for the flame area. *Combust. Sci. Technol.* **70**, 1–15.

Cant, R.S., Pope, S.B. & Bray, K.N.C. 1990 Modelling of flamelet surface-to-volume ratio in turbulent premixed combustion. *Proc. Combust. Inst.* **23**, 809–815.

Carroll, P.L. & Blanquart, G. 2016 A proposed modification to Lundgren's physical space velocity forcing method for isotropic turbulence. *Phys. Fluids* **25**, 105114.

Chakraborty, N. & Cant, S. 2004 Unsteady effects of strain rate and curvature on turbulent premixed flames in an inflow-outflow configuration. *Combust. Flame* **137** (1–2), 129–147.

Chakraborty, N., Hartung, G., Katragadda, M. & Kaminski, C.F. 2011 Comparison of 2D and 3D density-weighted displacement speed statistics and implications for laser based measurements of flame displacement speed using direct numerical simulation data. *Combust. Flame* **158**, 1372–1390.

Chakraborty, N., Kolla, H., Sankaran, R., Hawkes, E.R., Chen, J.H. & Swaminathan, N. 2013 Determination of three-dimensional quantities related to scalar dissipation rate and its transport from two-dimensional measurements: direct numerical simulation based validation. *Proc. Combust. Inst.* **34** (1), 1151–1162.

Chakraborty, N. & Swaminathan, N. 2007 Influence of the Damköhler number on turbulence-scalar interaction in premixed flames. I. Physical insight. *Phys. Fluids* **19**, 045103.

Chen, J.H., *et al.* 2009 Terascale direct numerical simulations of turbulent combustion using S3D. *Comput. Sci. Disc.* **2**, 015001.

Cifuentes, L., Dopazo, C., Martin, J. & Jimenez, C. 2014 Local flow topologies and scalar structures in a turbulent premixed flame. *Phys. Fluids* **26**, 065108.

Donbar, J.M., Driscoll, J.F. & Carter, C.D. 2001 Strain rates measured along the wrinkled flame contour within turbulent non-premixed jet flames. *Combust. Flame* **125**, 1239–1257.

Driscoll, J.F., Chen, J.H., Skiba, A.W., Carter, C.D., Hawkes, E.R. & Wang, H. 2020 Premixed flames subjected to extreme turbulence: some questions and recent answers. *Prog. Energy Combust. Sci.* **76**, 100802.

Dunn-Rankin, D. 2007 *Lean Combustion*. Academic Press.

Hartung, G., Hult, J., Balachandran, R., MacKley, M.R. & Kaminski, C.F. 2009 Flame front tracking in turbulent lean premixed flames using stereo PIV and time-sequenced planar LIF of OH. *Appl. Phys.* B **96** (4), 843–862.

HARTUNG, G., HULT, J., KAMINSKI, C.F., ROGERSON, J.W. & SWAMINATHAN, N. 2008 Effect of heat release on turbulence and scalar-turbulence interaction in premixed combustion. *Phys. Fluids* **20** (3), 035110.

HAWKES, E.R. & CANT, R.S. 2000 A flame surface density approach to large-eddy simulation of premixed turbulent combustion. *Proc. Combust. Inst.* **28**, 51–58.

HAWKES, E.R. & CANT, R.S. 2001 Implications of a flame surface density approach to large eddy simulation of premixed turbulent combustion. *Combust. Flame* **126**, 1617–1629.

HAWKES, E.R., SANKARAN, R. & CHEN, J.H. 2011 Estimates of the three-dimensional flame surface density and every term in its transport equation from two-dimensional measurements. *Proc. Combust. Inst.* **33** (1), 1447–1454.

HAWKES, E.R., SANKARAN, R., CHEN, J.H., KAISER, S.A. & FRANK, J.H. 2009 An analysis of lower-dimensional approximations to the scalar dissipation rate using direct numerical simulations of plane jet flames. *Proc. Combust. Inst.* **32 I** (1), 1455–1463.

KENNEDY, A. & CARPENTER, M.H. 1994 Several new numerical methods for compressible shear-layer simulations. *Appl. Numer. Maths* **14**, 397–433.

KENNEDY, C.A., CARPENTER, M.H. & LEWIS, R.M. 2000 Low-storage, explicit Runge–Kutta schemes for the compressible Navier–Stokes equations. *Appl. Numer. Maths* **35**, 177–219.

KIM, H.S. & PITSCH, H. 2007 Scalar gradient and small-scale structure in turbulent premixed combustion. *Phys. Fluids* **19**, 115104.

KOLLMANN, W. & CHEN, J.H. 1998 Pocket formation and the flame surface density equation. *Proc. Combust. Inst.* **27**, 927–934.

KULLBACK, S. & LEIBLER, R.A. 1951 On information and sufficiency. *Ann. Math. Statist.* **22**, 79–86.

LAPOINTE, S. & BLANQUART, G. 2017 A priori filtered chemical source term modeling for LES of high Karlovitz number premixed flames. *Combust. Flame* **176**, 500–510.

LEE, T., NORTH, G.L. & SANTAVICCA, D.A. 1992 Curvature and orientation statistics of turbulent premixed flame fronts. *Combust. Sci. Technol.* **84**, 121–132.

LIPATNIKOV, A.N., SABELNIKOV, V.A., HERNÁNDEZ-PÉREZ, F.E., SONG, W. & IM, H.G. 2020 A priori DNS study of applicability of flamelet concept to predicting mean concentrations of species in turbulent premixed flames at various Karlovitz numbers. *Combust. Flame* **222**, 370–382.

LU, T. & LAW, C.K. 2008 A criterion based on computational singular perturbation for the identification of quasi steady state species: a reduced mechanism for methane oxidation with NO chemistry. *Combust. Flame* **154** (4), 761–774.

LUCA, S., ATTILI, A., LO, E., CRETA, F. & BISETTI, F. 2019 On the statistics of flame stretch in turbulent premixed jet flames in the thin reaction zone regime at varying Reynolds number. *Proc. Combust. Inst.* **37** (2), 2451–2459.

LUO, Z., YOO, C.S., RICHARDSON, E.S., CHEN, J.H., LAW, C.K. & LU, T. 2012 Chemical explosive mode analysis for a turbulent lifted ethylene jet flame in highly-heated coflow. *Combust. Flame* **159** (1), 265–274.

MOHAMMADNEJAD, S., AN, Q., VENA, P., YUN, S. & KHEIRKHAH, S. 2020 Thick reaction zones in non-flamelet turbulent premixed combustion. *Combust. Flame* **222**, 285–304.

MOHAMMADNEJAD, S., VENA, P., YUN, S. & KHEIRKHAH, S. 2019 Internal structure of hydrogen-enriched methane–air turbulent premixed flames: flamelet and non-flamelet behavior. *Combust. Flame* **208**, 139–157.

NILSSON, T., LANGELLA, I., DOAN, N.A.K., SWAMINATHAN, N., YU, R. & BAI, X.S. 2019 A priori analysis of sub-grid variance of a reactive scalar using DNS data of high Ka flames. *Combust. Theor. Model.* **23** (5), 885–906.

NOMURA, K.K. & ELGHOBASHI, S.E. 1992 Mixing characteristics of an inhomogeneous scalar in isotropic and homogeneous sheared turbulence. *Phys. Fluids* A **4** (3), 606–625.

PASSOT, T. & POUQUET, A. 1987 Numerical simulation of compressible homogeneous flows in the turbulent regime. *J. Fluid Mech.* **181**, 441–466.

PETERS, N. 2000 *Turbulent Combustion*. Cambridge University Press.

POINSOT, T. & VEYNANTE, D. 2005 *Theoretical and Numerical Combustion*. R.T. Edwards.

POPE, S.B. 1988 The evolution of surfaces in turbulence. *Intl J. Engng Sci.* **26**, 445–469.

SANKARAN, R., HAWKES, E.R, CHEN, J.H, LU, T. & LAW, C.K. 2007 Structure of a spatially developing turbulent lean methane–air Bunsen flame. *Proc. Combust. Inst.* **31**, 1291–1298.

SANKARAN, R., HAWKES, E.R., YOO, C.S. & CHEN, J.H. 2015 Response of flame thickness and propagation speed under intense turbulence in spatially developing lean premixed methane-air jet flames. *Combust. Flame* **162** (9), 3294–3306.

SPONFELDNER, T., BOXX, I., BEYRAU, F., HARDALUPAS, Y., MEIER, W. & TAYLOR, A.M.K.P. 2015 On the alignment of fluid-dynamic principal strain-rates with the 3D flamelet-normal in a premixed turbulent V-flame. *Proc. Combust. Inst.* **35** (2), 1269–1276.

STEINBERG, A.M., CORITON, B. & FRANK, J.H. 2015 Influence of combustion on principal strain-rate transport in turbulent premixed flames. *Proc. Combust. Inst.* **35** (2), 1287–1294.

STEINBERG, A.M. & DRISCOLL, J.F. 2009 Straining and wrinkling processes during turbulence-premixed flame interaction measured using temporally-resolved diagnostics. *Combust. Flame* **156** (12), 2285–2306.

STEINBERG, A.M., DRISCOLL, J.F. & SWAMINATHAN, N. 2012 Statistics and dynamics of turbulence–flame alignment in premixed combustion. *Combust. Flame* **159**, 2576–2588.

SWAMINATHAN, N. & GROUT, R.W. 2006 Interaction of turbulence and scalar fields in premixed flames. *Phys. Fluids* **18**, 045102.

TANAHASHI, M., FUJIMURA, M. & MIYAUCHI, T. 2000 Coherent fine-scale eddies in turbulent premixed flames. *Proc. Combust. Inst.* **28**, 529–535.

TROUVE, A. & POINSOT, T. 1994 The evolution equation for the flame surface density in turbulent premixed combustion. *J. Fluid Mech.* **278**, 1–31.

TRUNK, P.J., BOXX, I., HEEGER, C., MEIER, W., BÖHM, B. & DREIZLER, A. 2013 Premixed flame propagation in turbulent flow by means of stereoscopic PIV and dual-plane OH-PLIF at sustained kHz repetition rates. *Proc. Combust. Inst.* **34** (2), 3565–3572.

VERVISCH, L., BIDAUX, E., BRAY, K.N.C. & KOLLMANN, W. 1995 Surface density function in premixed turbulent combustion modeling, similarities between probability density function and flame surface approaches. *Phys. Fluids* **7** (10), 2496–2503.

VEYNANTE, D., LODATO, G., DOMINGO, P., VERVISCH, L. & HAWKES, E.R. 2010*a* Estimation of three-dimensional flame surface densities from planar images in turbulent premixed combustion. *Exp. Fluids* **49** (1), 267–278.

VEYNANTE, D., LODATO, G., DOMINGO, P., VERVISCH, L. & HAWKES, E.R. 2010*b* Estimation of three-dimensional flame surface densities from planar images in turbulent premixed combustion. *Exp. Fluids* **49** (1), 267–278.

VEYNANTE, D. & VERVISCH, L. 2002 Turbulent combustion modeling. *Prog. Energy Combust. Sci.* **28**, 193–266.

WANG, H., HAWKES, E.R. & CHEN, J.H. 2016 Turbulence-flame interactions in DNS of a laboratory high Karlovitz premixed turbulent jet flame. *Phys. Fluids* **28**, 095107.

WANG, H., HAWKES, E.R. & CHEN, J.H. 2017*a* A direct numerical simulation study of flame structure and stabilization of an experimental high Ka CH_4/air premixed jet flame. *Combust. Flame* **180**, 110–123.

WANG, H., HAWKES, E.R., CHEN, J.H., ZHOU, B., LI, Z. & ALDÉN, M. 2017*b* Direct numerical simulations of a high Karlovitz number laboratory premixed jet flame – an analysis of flame stretch and flame thickening. *J. Fluid Mech.* **815**, 511–536.

WANG, H., HAWKES, E.R., SAVARD, B. & CHEN, J.H. 2018 Direct numerical simulation of a high Ka CH_4/air stratified premixed jet flame. *Combust. Flame* **193**, 229–245.

WANG, H., HAWKES, E.R., ZHOU, B., CHEN, J.H., LI, Z. & ALDÉN, M. 2017*c* A comparison between direct numerical simulation and experiment of the turbulent burning velocity-related statistics in a turbulent methane-air premixed jet flame at high Karlovitz number. *Proc. Combust. Inst.* **36** (2), 2045–2053.

WANG, J., ZHANG, M., HUANG, Z., KUDO, T. & KOBAYASHI, H. 2013 Measurement of the instantaneous flame front structure of syngas turbulent premixed flames at high pressure. *Combust. Flame* **160** (11), 2434–2441.

YOO, C.S. & IM, H.G. 2007 Characteristic boundary conditions for simulations of compressible reacting flows with multi-dimensional, viscous and reaction effects. *Combust. Theor. Model.* **11** (734), 259–286.

ZHANG, Q., SHANBHOGUE, S.J., LIEUWEN, T. & O'CONNOR, J. 2011 Strain characteristics near the flame attachment point in a swirling flow. *Combust. Sci. Technol.* **183** (7), 665–685.